CrossMark

Optical and electrical properties of nanostructured *N,N′*-diphenyl-*N,N′*-di-*p*-tolylbenzene-1,4-diamine organic thin films

A. El-ghandour[1] · Mohamed Farhat O. Hameed[1,2,3] · A. S. Awed[4] · S. S. A. Obayya[1]

Abstract

In this paper, we introduce an extensive study on nanostructured thin films of an organic small molecule *N,N′*-diphenyl-*N,N′*-di-*p*-tolylbenzene-1,4-diamine, (NTD). Further, the possibility of using NTD as a hole transport layer in optoelectronic devices is reported for the first time to the best of our knowledge. In this context, the thermal behaviour, crystal structure, optical absorption in ultraviolet–visible regions, and DC electrical conductivity of the as-deposited NTD thin films are investigated. The differential scanning calorimetry (DSC) investigations show that NTD has a phase transition at a high temperature of 190 °C which may not affect its morphological stability. Further, the XRD patterns reveal that NTD thin films have an as-amorphous nature with some crystals. Additionally, optical investigations indicate that the indirect electronic transition from valence to conduction band is the most probable transition which agrees well with the amorphous structure of NTD thin films. The value of the mobility gap decreases from 2.74 to 2.51 eV when the thickness of the films increases from 80 to 200 nm. Furthermore, the absorbance lies below 370 nm and the thinnest film of thickness 80 nm achieves the highest absorbance. Further, the DC electrical measurements show that the NTD film has an activation energy of 378 meV. The DC conductivity is interpreted in terms of the variable range hopping (VRH) model. Based on our studies, NTD thin films are proposed with thickness range 50–80 nm to serve as a hole transport layer in white organic light emitting diodes (OLEDs).

1 Introduction

In the last two decades, the studies of organic semiconductors have increased due to their electronic and optoelectronic properties [1, 2]. The structure of organic semiconducting molecules (OSMs) can be easily modified, resulting in new molecules with tuneable structural, thermal, optical and electrical properties [3]. OSMs are used in different applications including organic light emitting diodes (OLEDs) [3], organic thin film transistors (OFETs) [4] and organic solar cells (OSCs) [5–7].

Particularly, OLEDs have attracted great attention because they reduce the operating voltage, consume less energy and improve the efficiency of the device's electroluminescence (EL) [8]. Additionally, they have high potential for mass production with low cost. The OLEDs can be fabricated by using polymers or OSMs [8]. The OLEDs are usually produced by sandwiching an emissive organic layer between two organic layers [8]. The first layer serves as a hole transport layer (HTL), while the other layer acts as an electron transport layer (ETL) where the three layers are sandwiched between two electrodes [9].

Each layer of the OLEDs plays a certain role in the operation process [10]. The HTL layer injects holes to the organic emissive layer and ensures hole blocking at the ETL [11]. Udhiarto et al. [12] have studied the effect of HTL thickness on the performance of the OLED. It has been shown that the performance of the OLED is enhanced as a function of the HTL thickness [12]. In this context, each 1 nm of HTL layer can balance the charge concentration between free holes and electrons in the emissive layer. Also, Lim et al. [13] have studied the optical and electrical properties

✉ Mohamed Farhat O. Hameed
   mfarahat@zewailcity.edu.eg

✉ S. S. A. Obayya
   sobayya@zewailcity.edu.eg

1 Center for Photonics and Smart Materials, Zewail City
   of Science and Technology, 6th October, Giza, Egypt

2 Nanotechnology Engineering Program, University of Science
   and Technology, Zewail City of Science and Technology,
   6th October, Giza, Egypt

3 Faculty of Engineering, Mansoura University, Mansoura,
   Egypt

4 Department of Physics, Faculty of Science, Damietta
   University, New Damietta, Egypt

of the *N,N*₀-diphenyl-*N,N*₀-bis(1-naphthyl)-[1,10-biphthyl]-4,40-diamine (NPB) thin films as a hole transport layer. In this regard, the energy gap decreases when the layer thickness increases, while the electrical conductivity is dependent on the thickness. Narayan et al. [14] have investigated the effect of thickness variation of copper (II) phthalocyanine as hole injection layer and 2,9 dimethyl-4,7-diphenyl-1,10-phenanthroline as a hole blocking layer with optimum thickness of 18 and 10 nm, respectively.

N,N′-diphenyl-*N,N′*-di-*p*-tolylbenzene-1,4-diamine, NTD, belongs to bis-amine molecules with low molecular weight. Additionally, bis-amine molecules are considered as the fundamental block in dendrimer polymers [15]. The dendrimers are crystallized with amorphous morphology [16]. Recently, dendrimer materials have been extensively studied because they contain bis-aromatic amine that can trap metal ions within the voids in the dendrimers and form new types of organic–metallic hybrid nanomaterials [15]. Thin films of such low molecular weight compounds can be obtained by sublimation under high vacuum. Further, they can be used for electronic devices such as organic field-effect transistors and OLEDs [17].

The efficiency of OLEDs can be maximized by optimizing the charge balancing-based modulating hole injection and hole mobility [14]. In the present work, we introduce NTD as a novel hole transport layer for the first time to the best of our knowledge. Thermal evaporation technique is used to deposit NTD powder into thin films with thicknesses of 80, 120, 160, and 200 nm. The thermal investigations show that NTD has a high glass transition temperature $T_g = 190$ °C, which is higher than that of widely used NPB prepared by Lim et al. [13]. The optical properties of the pristine NTD thin films with different thicknesses are also studied. The thinnest film (80 nm) achieves absorbance values comparable to that of the well-known hole transport layers, *N;N*₀-diphenyl-*N; N*₀-bis(3-methyl-phenyl)-(1; 10-biphenyl)-4; 40-diamine (TPD) and NPB presented in [13, 18]. Furthermore, the obtained energy gaps decrease on increasing the NTD thickness, which agrees well with those reported in [13] for NPB. NTD also shows an electrical conductivity, σ_{dc}, that is higher than that of MeO-S-TPD [18] and comparable with that reported for PV-TPD [19], PV-TPDoM [20], and Di-NPB [13].

2 Experimental details

2.1 Materials

An organic small molecule *N,N′*-diphenyl-*N,N′*-di-*p*-tolylbenzene-1,4-diamine, NTD, is purchased from Sigma Aldrich in a powder form with purity of 99.99%. The NTD powder appears white with empirical formula $C_{32}H_{28}N_2$.

NTD molecular weight is 440.50 g/mol with density of 1.250 g cm⁻³. The molecular structure of NTD is presented in Fig. 1.

2.2 Nanostructured thin film synthesis and characterization

Thin films of NTD are successfully deposited by the thermal evaporation technique (Edwards Co., England, model E 306 A) [21] under a pressure of about 10^{-5} Pa by using a high vacuum coating unit. The NTD powder is deposited onto pre-cleaned glass substrates for structure analysis, while pre-cleaned flat fused quartz substrates are used for optical investigation where both substrates are maintained at room temperature. We prepared four films of different thicknesses 80, 120, 160 and 200 nm, with a deposition rate of 2.5 (nm/s) controlled by a quartz crystal thickness monitor (Model, TM-350 MAXTEK, and Inc. USA). Further, thermal analysis is performed using differential scanning calorimeter DSC-60 by Shimadzu, Japan. The DSC analysis is carried out under nitrogen atmosphere with a flow rate of 50 ml min⁻¹. The measurement is recorded in temperature range from 10 up to 300 °C at an average heating of 5 °C min⁻¹ with 12.5 mg sample weight. Also, Fourier transform infrared (FT-IR) spectroscopy was performed using a FT-IR 3600 infrared spectrometer (Jasco, USA) using a KBr pellet as a reference. The crystal structure of NTD powder and the as-deposited thin films are investigated using X-ray diffraction (XRD; Shimadzu XRD-6000, Japan). The XRD patterns are obtained in the range of 2θ from 4° to 90° at room temperature. The Cu Kα is used as a radiation source of wavelength $\lambda = 0.15408$ nm, with scan rate 2°/min, operation voltage 50 kV and current of 40 mA [22]. The absorbance $A(\lambda)$, the transmittance $T(\lambda)$, and the reflectance $R(\lambda)$ for different thicknesses of as-deposited NTD thin films are measured in the wavelength range 200–2400 nm via a double beam spectrophotometer (JASCO model V-570 UV–Vis–NIR) [23]. The measured values of $T(\lambda)$ and $R(\lambda)$ are computed via a software program privately developed to calculate the refractive index and extinction coefficient. A device of the structure Au/NTD/Au is thermally evaporated to investigate the direct electrical
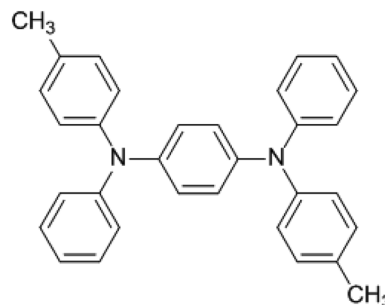

Fig. 1 Molecular structure of NTD

conductivity σ_{dc}. NTD is sublimated from a quartz crucible heated by a molybdenum heater. The vacuum inside the evaporation chamber is kept at 5×10^{-5} mbar during the deposition. The gold electrodes are thermally evaporated directly from a molybdenum filament [24]. The deposition rate and the thickness are equal to 25 A°/s and 80 nm, respectively. All measurements are performed at different temperatures in air under dark conditions. The electrical resistance is measured as a function of temperature using Keithley 2635 A high impedance electrometer. The temperature measurements of the film are carried out in the range of 338–463 K using the NiCr–NiAl thermocouple [25].

3 Theory

The structural parameters such as the average crystallite size, D, the average dislocation density, δ, the average inter-separation distance, Y, and stacking fault (SF) can be calculated from the broadening width (β) of the most intensive peak with the aid of Debye–Scherer formula according to the following relations [26]:

$$D = \frac{0.94\lambda}{\beta \cos(\theta)}, \tag{1}$$

$$\delta = \frac{1}{D^2}, \tag{2}$$

$$Y = \frac{5\lambda}{8 \sin \theta}, \tag{3}$$

$$SF = \frac{2\pi^2 \beta}{45\sqrt{3} \tan \theta}, \tag{4}$$

where θ is the diffraction angle, λ is the wavelength of the incident X-ray photons and β is the broadening width of the Bragg peak which relies on instrument- and sample-dependent effects. To avoid these contributions, it is necessary to collect a diffraction pattern from the line broadening of a standard material such as the bulk structure to determine the instrumental broadening. Then, the instrument-corrected broadening follows the relation: $\beta = [(\beta^2)_{measured} - (\beta^2)_{instrumental}]^{1/2}$ [27, 28].

The absorption coefficient, $\alpha (\lambda)$, can be calculated using the measured absorbance $A (\lambda)$ according to the relation [29]:

$$\alpha(\lambda) = \frac{2.303 \, A(\lambda)}{d}, \tag{5}$$

where d is the thickness of the measured thin films. The calculated $\alpha (\lambda)$ are used to study the optical transitions and the energy gaps by using the following equation [30]:

$$\alpha h\nu = B(h\nu - E_g)^q, \tag{6}$$

where $h\nu$ is the photon energy of the incident light, B is a constant, E_g is the energy gap, and the exponent q is a constant based on the type of transition. In this context, $q = 2$ or 3 for indirect allowed and forbidden transitions, respectively. However, $q = 1/2$ or 3/2 for direct allowed and forbidden transitions, respectively.

The refractive index, n, and the extinction coefficient, k, of the prepared films can be also calculated by using the following equations [31–33]:

$$n = \left(\frac{4R}{(1-R)^2} - k^2 \right)^{1/2} + \left(\frac{1+R}{1-R} \right), \tag{7}$$

$$k = \frac{\alpha\lambda}{4\pi}, \tag{8}$$

where $T (\lambda)$ and $R (\lambda)$ are the measured transmission and reflectance, respectively.

The refractive index is related to the dielectric constant, ε_∞, and the ratio N/m* by the following relation [34]:

$$n^2 = \varepsilon_L - \left(\frac{e^2}{4\pi^2 \varepsilon_o C^2} \right) \left(\frac{N_{opt}}{m^*} \right) \lambda^2, \tag{9}$$

where ε_L is the real part of the dielectric constant, e is the electronic charge, ε_o is the permittivity of the free space, c is the speed of light waves, Nopt is the number of carriers and m^* is the effective mass of the charge carriers. The relation between the free-electron relaxation time, τ, the imaginary part, ε_2, of the dielectric constant and the wavelength of the incident photons is given by [35]:

$$\varepsilon_2 = \frac{1}{4\pi^3 \varepsilon_o} \left(\frac{e^2}{c^3} \right) \left(\frac{N_{opt}}{m^*} \right) \left(\frac{1}{\tau} \right) \lambda^3 . \tag{10}$$

Additionally, the optical resistivity ρ_{opt} can be obtained based on the optical mobility, μ_{opt}, and the number of charge carriers as expressed by [36]:

$$\mu_{opt} = \frac{e\tau}{m^*} , \tag{11}$$

$$\rho_{opt} = \frac{1}{e\mu_{opt}N_{opt}} , \tag{12}$$

where $m^* = 0.44 m_o$ and m_o is the mass of the electron.

The direct electrical conductivity, σ_{dc}, of a material is related to the measured electrical resistance and its dimensions as given by [37]:

$$\sigma_{dc} = \frac{l}{RA} , \tag{13}$$

where, l, A and R are the length, area and measured electrical resistance of the sample, respectively. In hopping conduction, the σ_{dc} for semiconductor materials depends on the temperature and obeys Arrhenius' relation [38]:

$$\sigma_{dc} = \sigma_o \exp\left(\frac{-\Delta E_{dc}}{K_B T}\right), \tag{14}$$

where σ_o is the pre-exponential factor which includes the charge carrier mobility and the density of states, ΔE_{dc} is the activation energy for hopping conduction, k_B is Boltzmann's constant and T is the absolute temperature.

σ_{dc} that follows the Mott's variable range hopping (VRH) model can be taken as [39, 40]:

$$\sigma_{dc} = \sigma_o \exp\left(-\frac{T_o}{T}\right)^p, \tag{15}$$

$$T_o = \frac{24}{[\pi k_B Z^3 N(E_F)]}, \tag{16}$$

where σ_o is the pre-exponential factor, p is an exponent which can be 1/4, 1/3 or ½ for different materials [40], T_o is the characteristic temperature, $N(E_F)$ is the number of delocalized energy states at Fermi level and Z is the decay constant of the localized wave function which equals to 10^7 cm^{-1} [41].

According to the VRH model, it is possible to investigate the hopping distance, R_{hop}, and the hopping energy, W_{hop}, at a certain temperature by using the following relations [41, 42]:

$$R_{hop} = \frac{Z^{1/4}}{[8\pi k_B T N(E_F)]^{1/4}}, \tag{17}$$

$$W_{hop} = 0.5 K_B T_o^{0.5} T^{0.5}. \tag{18}$$

4 Results and discussion

4.1 Structure analysis

In this study, the thermal changes of NTD thin films, thermally evaporated on a glass substrate, are successfully detected by deferential scanning calorimetry, DSC, in air. Figure 2 presents the DSC thermogram for NTD thin film in the temperature range 10–300 °C. It is noticed from this figure that NTD has thermal stability in a wide temperature range 30–185 °C. Additionally, the first endothermic peak appears at $T = 190$ °C which can be attributed to the melting temperature. The high melting temperature of NTD indicates the stability of its morphology at high operating
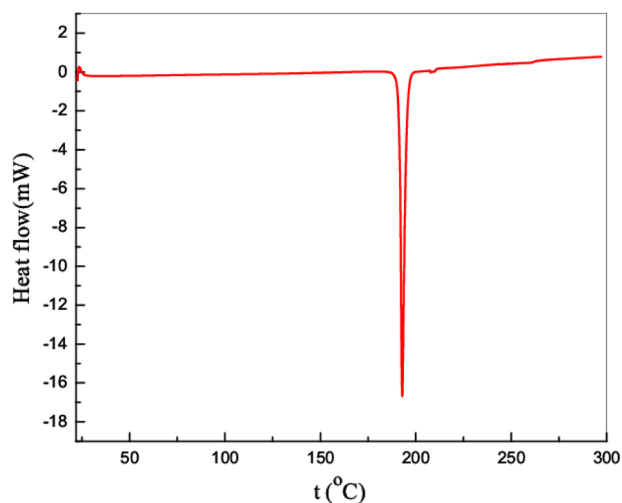

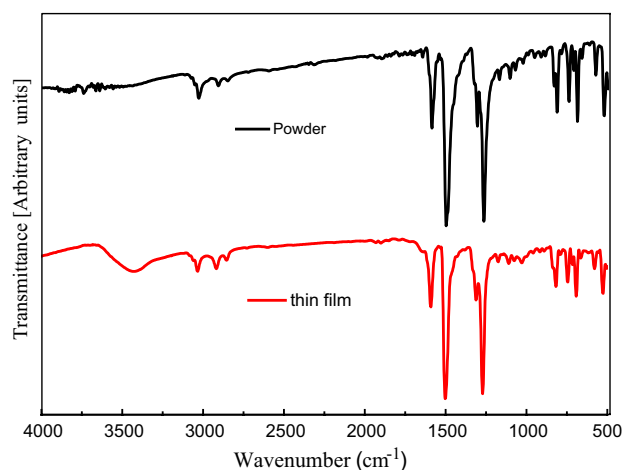**Fig. 2** DSC thermogram of NTD thin film

Fig. 3 FTIR spectra of the powder and the pristine NTD thin film

temperatures. NTD shows an enhanced morphological stability in comparison to the previously reported HTL molecules such as PV-TPD [18], PV-TPDoM [20] and Di-NPB [19].

Organic molecule bonds can be stretched and bent upon absorption of infrared irradiation, IR, in the range of 400–4000 cm^{-1} [43]. In this investigation, Fourier transform Infrared (FTIR) spectroscopy is used to identify functional groups and define the molecular structure of the prepared materials to show the effects of preparation techniques [44]. Figure 3 shows the FTIR spectra of the powder and the pristine NTD thin film of thickness 80 nm. It may be seen from this figure that there is no significant change in the chemical bonding structure of the powder compared to the structure of the pristine thin film. The stability of the chemical structure indicates that the thermal evaporation technique is suitable

for NTD thin film preparation. The possible vibrational modes for the NTD are assigned and listed in Table 1.

The crystal structures of as-purchased powder and as-deposited NTD thin film of thickness 80 nm are also studied using the XRD technique. Figure 4a presents the XRD patterns of the NTD powder. It is observed that the powder of NTD exhibits a polycrystalline phase with many peaks with different intensities. The diffraction peaks in the powder spectrum are indexed [45], the lattice parameters are obtained and the crystal system is defined with the aid of CRYSFIRE computer program [30]. The values of Miller indices, $h\ k\ l$, for each diffraction peak are calculated using CHEKCELL computer program [30]. The obtained results indicate that the NTD powder has a triclinic crystal system with a space group P1 and the lattice parameters are $a = 9.588$ Å, $b = 18.793$ Å, $c = 8.879$ Å, $a = 93.850$, $\beta = 112.750$ and $\gamma = 81.500$. Figure 4b illustrates the XRD pattern of as-deposited NTD thin film. It is noticed that the film has an amorphous structure with some crystals. The film shows three diffraction peaks at $2\theta = 14.26$, 20.21 and 21.58 corresponding to diffraction from the planes $(0\bar{3}0)$, $(\bar{1}02)$, $(2\bar{1}0)$, respectively. It should be noted that some particles of the powder underwent selective crystallization which is evident from the preferred orientation on the planes $(0\bar{3}0)$, $(\bar{1}02)$, $(2\bar{1}0)$, as depicted in Fig. 4a. Moreover, the film's surface grows with good homogeneity and the thickness of the NTD film is high. Therefore, the X-rays do not penetrate the film with no peaks due to the substrate. In this context, if there are peaks in the XRD pattern due to the substrate, there must be a 'hump' in the diffraction pattern (comes from the glass substrate) as reported in [46].

The average values of crystallite size, D, inter-separation distance, Y, stacking fault, SF, and the dislocation density, δ, for as-deposited NTD thin film of thickness 80 nm are calculated and found to be 35.55 nm, 7.94 Å, 0.027 and 0.31×10^{-3} Lines/nm², respectively.

In the current study, the optical properties of the NTD thin films are characterized as a hole transport layer (HTL) in OLEDs. It is worth nothing that the transport materials
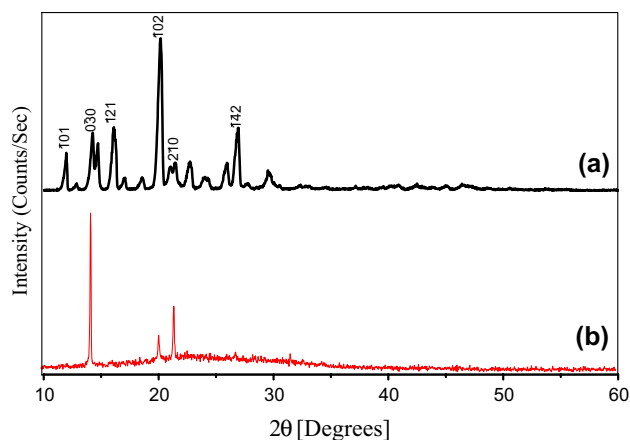

Fig. 4 X-ray diffraction patterns of **a** the powder of NTD and **b** the pristine thin film

have an absorption in the visible range. Therefore, the HTL thickness should be optimized to confine holes to the recombination zone in an emitting material layer (EML). The optical characterizations for different thickness of as-deposited NTD thin films are investigated by measuring the absorbance A (λ), the transmittance T (λ), and the reflectance R (λ). The spectrum of A (λ) as a function of the incident light wavelength, through the range of 200–1000 nm, is presented in Fig. 5. In general, it is observed that the different thicknesses of the as-deposited NTD thin films show a dominant absorption in the wavelength range 200–370 nm below the edge of the visible light range. Furthermore, the absorption increases by decreasing the thickness of the thin films. The thinnest film of thickness 80 nm has the highest absorption with an intense broad peak at $\lambda = 350$ nm. Based on

Table 1 FTIR assignment of the NTD powder and as-deposited thin film of 80 nm thickness

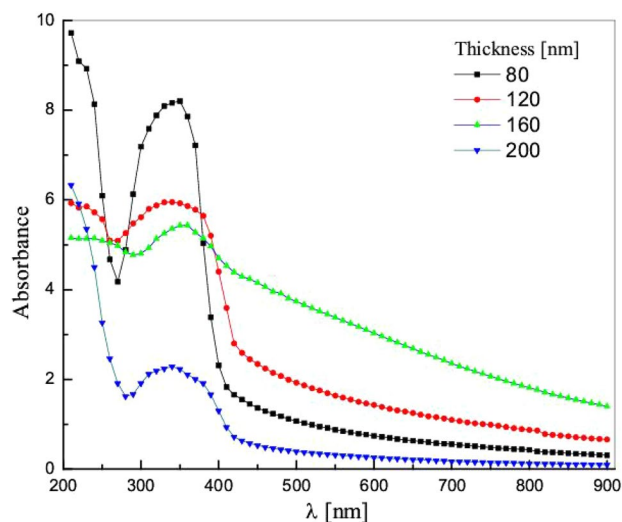| Wavenumber, $\bar{v}$, (cm⁻¹)		Assignments
Powder	Pristine thin film	
3034	3030	C–H stretching, aromatic
2912	2918	CH₃ stretching, aromatic
2855	2855	C–H aromatic
1597	1590	C=C asymmetric, aromatic
1500	1501	C–C stretching, aromatic
1306	1310	C-N stretching, aromatic
1262	1272	C–N stretching, aromatic

Fig. 5 Thickness dependence of the absorbance as a function of the incident wavelengths
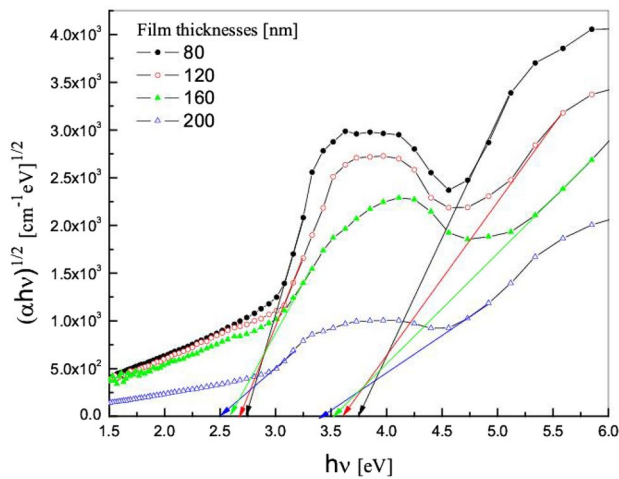
Fig. 6 Variation of $(\alpha h\nu)^{1/2}$ as a function of the incident photon energy, $h\nu$, for the different thicknesses of NTD thin films

Table 2 Energy gaps of different thicknesses of NTD thin films

Film thickness (nm)	Onset energy gap (eV)	Optical energy gap (eV)
80	2.74	3.75
120	2.68	3.60
160	2.60	3.51
200	2.51	3.41

the observed low range of absorption, the NTD thin films can be used as a hole transport layer in OLEDs [6, 20] and OSCs [47–49].

4.2 Absorption and dielectric properties

The dependence of $(\alpha h\nu)^{1/q}$ on the photon energy ($h\nu$) for the optical bandgap is also studied. It has been found that the indirect allowed transition is the most probable transition with $q = 2$. According to [21], the indirect transitions in organic semiconductors are the preferred transitions due to the non-crystalline structure of those materials. The relation between $(\alpha h\nu)^{1/2}$ and ($h\nu$) for the different thicknesses of as-deposited NTD thin films is illustrated in Fig. 6. The intercept of the straight-line graphs with the abscissa axis gives the values of the energy gaps which are obtained and listed in Table 2.

It is evident from Fig. 6 that the energy bandgap increases with decrease in the thin films' thickness due to the absence of charge accumulation at the grain boundaries, which agrees well with that reported in [50, 51]. Further, NTD has a wide bandgap with no absorption in the visible range of the solar spectrum. Therefore, NTD is more suitable as a transparent
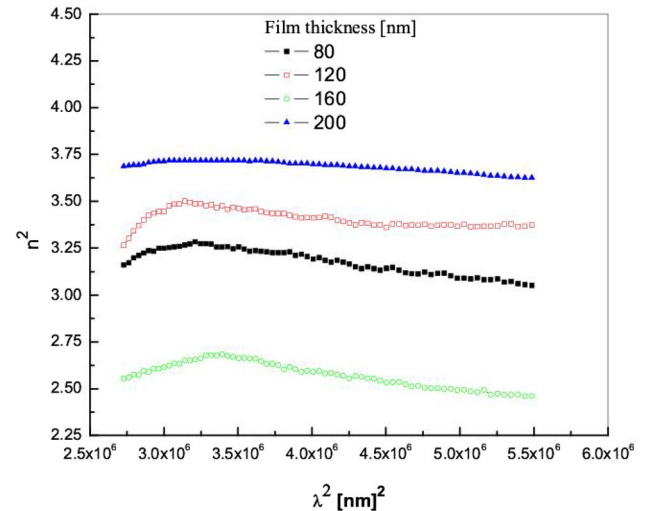

Fig. 7 The relation between the squared refractive index, n^2, and the incident wavelength, λ^2, for different thicknesses of NTD thin films

Table 3 Dispersion parameters for the different thicknesses of the NTD thin films

Film thickness (nm)	High frequency dielectric, ε_∞	The ratio (N/m^*) $\times 10^{56}$ [m^{-3} Kg^{-1}]
80	3.60	1.29
120	3.68	0.58
160	3.03	1.32
200	3.87	0.53

transport layer as mentioned earlier. In Table 2, the onset energy gap refers to the beginning of optical absorption and formation of Frenkel exciton, or the formation of a bound electron–hole pair [21]. Additionally, the second energy value is the fundamental energy gap which is the energy gap between the valence band π–band and conduction band π^*–band [52].

The refractive index data can be used to calculate the ratio of the charge carrier concentrations to the effective mass, N_{opt}/m^*, and the high frequency dielectric constant, ε_∞, by using the free carriers contribution and the dispersion vibration modes [36]. Figure 7 depicts the relation of the straight line between the square of the refractive index, n^2, and the square of the incident wavelength value, λ^2, for NTD thin films of different thicknesses. The slope of that line is used to calculate the number of charge carriers per effective mass N_{opt}/m^*. Also, the extrapolation of this line equals to the high frequency dielectric constant, ε_∞. The values of N_{opt}/m^* and ε_∞ for different thicknesses are calculated and listed in Table 3.

The free-electron relaxation time, τ, can be used to determine the dielectric function which is an important property for the design of optical devices [36]. Figure 8 shows a plot

of ε_2 versus λ^3 which results in a straight line with a slope of $\left[\frac{1}{4\pi^3\varepsilon_o}\left(\frac{e^2}{c^3}\right)\left(\frac{N_{opt}}{m^*}\right)\left(\frac{1}{\tau}\right)\right]$. The values of the relaxation times τ for different thicknesses of as-deposited NTD thin films are calculated and listed in Table 4. It is found that the thinnest film, 80 nm, has the shortest relaxation time of 8.5 Fs. The electrical properties of materials depend on their optical and structural properties [34]. The optical mobility μ_{opt} can be given as a function of the free relaxation time and the optical resistivity. The values of optical mobility, μ_{opt}, and optical resistivity, ρ_{opt}, for different thicknesses of NTD thin films are calculated and listed in Table 4.

4.3 DC conductivity

Studying the direct current electrical conductivity (σ_{dc}) gives valuable information to understand the conduction mechanisms in materials. In hopping conduction model, the conduction process occurs through the neighboring sites, and hence the hopping range and activation energy are independent on the temperature [39]. From Eq. 15, materials that follow the hopping conduction mechanism should have a linear relationship with $(1/T)^p$ [39]. The calculated values of $\ln(\sigma_{dc})$ are plotted as a function of the inverse of temperature ($1000/T$) and are presented in Fig. 9. It may be seen from this figure that $\ln(\sigma_{dc})$ increases as temperature increases. Additionally, the activation energy equals to 378 meV.

Based on the hypotheses of the VRH conduction model, the hopping range may vary as the temperature decreases. Moreover, the VRH model can describe the experimental data at low temperatures where charges transfer can occur through the nearest sites. From Eq. 15, materials that have
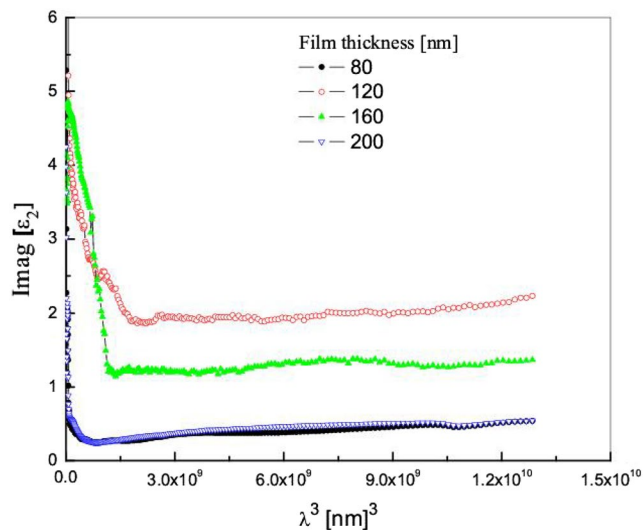
Table 4 Optoelctrical parameters of different thicknesses of NTD thin films

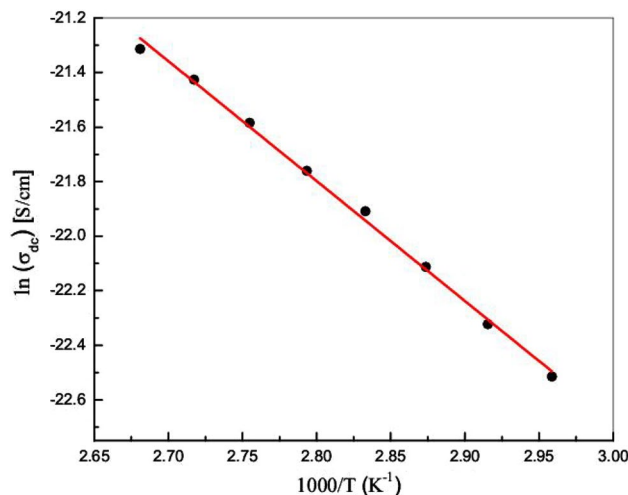| Film thickness [nm]	Relaxation time $\tau \times 10^{-14}$ (S)	Optical mobility $\mu_{opt} \times 10^{-3}$	Optical resistivity $\rho_{opt} \times 10^{-5}$
80	0.855	3.41	2.09
120	1.43	5.71	0.73
160	1.49	5.95	1.12
200	1.06	4.26	1.34

Fig. 9 The temperature dependence of the σ_{dc} for 80 nm NTD thin film

linear relationship between $\ln(\sigma_{dc})$ and $(1/T)^p$ obey the VRH conduction mechanism [39] and this model dominates when $T_o > 10^3$ (K) and $W > 3KT$ (eV) [39]. In the present work, the most probable value of "p" is equal to 1/2. Figure 10

Fig. 8 The variation of the imaginary part of the dielectric, ε_2, with the incident wavelengths λ^3 for different thicknesses of NTD thin films
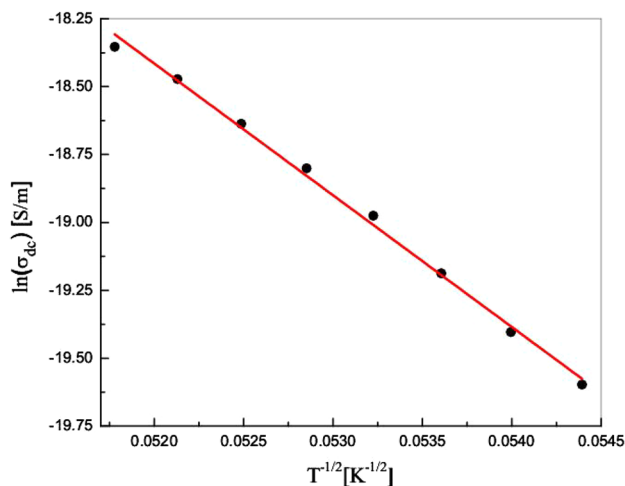

Fig. 10 The relation between $\ln(\sigma_{dc})$ and the reciprocal of the square root of absolute temperature for 80 nm NTD thin film
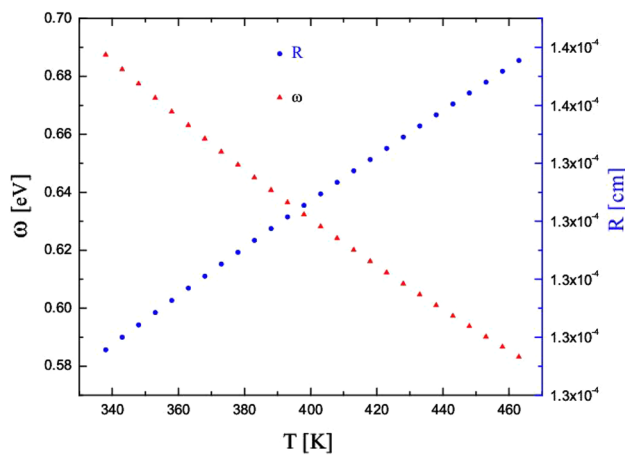
Fig. 11 The variation of the hopping energy, ω, and the hopping distance, R, as a function of the temperature for 80 nm NTD thin film

shows the temperature dependence of ln (σ_{dc}) with respect to $(1/T)^{-1/2}$ for NTD thin film. From the fitted line in Fig. 10, T_o equals to 2.34×10^5 K which is substituted in Eq. 14 to calculate the $N(E_F)$ of 3.8×10^{22} eV^{-1} cm^{-1}.

Figure 11 shows the hopping energy and hopping distance as a function of the temperature. It is observed that W_{hop} increases from 0.585 to 0.684 eV and R_{hop} decreases from 1.37×10^{-4} to 1.27×10^{-4} cm as temperature increases from 338 to 463 K.

The performance of the reported HTL (NTD) is compared to other HTLs in the literature to clarify the advantage of the present work over the preceding ones as shown in Table 5. The table illustrates the bandgap energy, glass transition, position of the absorption peak and electrical conductivity of the previously reported and current HTLs. It may be seen from this table that the reported HTL has the highest glass transition. Therefore, it is supposed to be morphologically stable under operation conditions of OLEDs, solar cells [49, 53] and other photovoltaic devices [54, 55]. Further, the reported HTL shows a strong absorption peak at 350 nm which is lower than any of the previously reported HTLs. Consequently, the present HTL will not decrease the efficiency of the solar cell noticeably. However, the presented

HTL has energy gap that is smaller than those previously reported in [12, 19, 20]. Furthermore, the conductivity of the reported HTL is comparable with that previously reported in the literature [11, 20].

5 Conclusion

The powder of NTD is thermally evaporated into thin films of different thicknesses. Thermal investigations show that NTD has a high $T_g = 190$ °C which implies that the morphology of NTD is stable at high operating temperatures. Structural investigations revealed that NTD film has amorphous structure with average crystal size of 35 nm. The optical studies also show that the absorbance of NTD thin films lies in the UV region, which suggests that NTD acts as a transparent hole transport layer in optoelectronic devices such as OLEDs and OSCs. Additionally, the thinnest film of thickness 80 nm has the highest absorption and the values of the energy bandgaps decreases as thickness increases. Further, the electrical studies show that the direct conductivity of NTD films increases as temperature increases and the conduction mechanism is interpreted in terms of hopping model. Additionally, it is found that hopping energy, W_{hop}, increases from 0.585 to 0.684 eV and the hopping distance, R_{hop}, decreases from 1.37×10^{-4} to 1.27×10^{-4} cm as temperature increases from 338 to 463 K.

Table 5 Comparison between the previously studied HTL materials and the novel NTD which is suggested in the present work

No.	Name	E_g (eV)	T_g (°C)	Abs. peak position (nm)	The σ_{dc} $\times 10^{-6}$[S/cm]
1	PV-TPD [19]	2.77	118.2	395	4.43
2	PV-TPDoM [18]	2.74	117.5	392	4.71
3	Di-NPB [19]	2.89	157.8	372	5.38
4	MeO-S-TPD [20]	2.87	115.7	387	34.5
5	This work	2.74	190	350	1.52

References

1. L. Dou, Y. Liu, Z. Hong, G. Li, Y. Yang, Chem. Rev. **115**, 12633 (2015)
2. T.M. Figueira-Duarte, K. Müllen, Chem. Rev. **111**, 7260 (2011)
3. C. Garcias-Morales, D. Romero-Borja, J.L. Maldonado, A.E. Roa, M. Rodríguez, J.P. García-Merinos, A. Ariza-Castolo, Molecules **22**, 1607 (2017)
4. H. Sirringhaus, Adv. Mater. **26**, 1319 (2014)
5. N.F.F. Areed, M.F.O. Hameed, M. Hussein, S.S.A. Obayya, IET Optoelectron. **8**, 167 (2014)
6. A. Mishra, P. Bäuerle, Angew. Chemie Int. Ed. **51**, 2020 (2012)
7. S.S. A., M.A. O. Doha, M.F.O. Rahman, Hameed, Opt. Quantum Electron. **47**, 1443 (2015)
8. K. Hutchison, J. Gao, G. Schick, Y. Rubin, F. Wudl, J. Am. Chem. Soc. **121**, 5611 (1999)
9. J. Blochwitz, M. Pfeiffer, T. Fritz, K. Leo, J. Blochwitz, M. Pfeiffer, T. Fritz, K. Leo, Appl. Phys. Lett. **729**, 67 (2012)
10. Q. Huang, J. Li, G.A. Evrnenenko, P. Dutta, T.J. Marks, Chem. Mater. **18**, 2431 (2006)
11. Z.C.H.L.M. Peysokhan, J. Nanophotonics 8, 08099 (2014)
12. A. Udhiarto, Y. Sister, S. Rini, M. Asvial, B. Munir, Int. Conf. Qual. Res. pp. 137–140 (2015)
13. M.Y. Lim, W.M.M. Yunus, Z.A. Talib, A. Kassim, C.F. Dee, A. Ismail, Am. J. Eng. Appl. Sci. **3**, 64 (2010)
14. K. Narayan, S. Varadharajaperumal, G. Mohan Rao, M. Manoj, Varma, T. Srinivas, Curr. Appl. Phys. **13**, 18 (2013)

15. A.S. Al-Fahdawi, H.A. Al-Kafajy, M.J. Al-Jeboori, S.J. Coles, C. Wilson, H. Potgieter, Acta Crystallogr. Sect. E Struct. Rep. Online **70**, 2 (2014)

16. Y. Sakamoto, T. Suzuki, A. Miura, H. Fujikawa, S. Tokito, Y. Taga, J. Am. Chem. Soc. **122**, 1832 (2000)

17. R.H. Friend, R.W. Gymer, A.B. Holmes, J.H. Burroughes, R.N. Marks, C. Taliani, D.D.C. Bradley, D.A. Dos Santos, J.L. Brédas, M. Lögdlund, W.R. Salaneck, Nature **397**, 121 (1999)

18. I. Vragović, E.M. Calzado, M.A. Díaz García, C. Himcinschi, L. Gisslén, R. Scholz, J. Lumin. **128**, 845 (2008)

19. D. Kajiya, K. Saitow, Int. Conf. Optoelectron. pp. 1–2, (2012)

20. S. Pfuetzner, A. Petrich, C. Malbrich, J. Meiss, M. Koch, M.K. Riede, M. Pfeiffer, K. Leo, Proc.of Spie **6999**, 69991M (2008)

21. I.S. Yahia, Y.S. Rammah, S. Alfaify, F. Yakuphanoglu, Superlattices Microstruct. **64**, 58 (2013)

22. M. Arshad, A. Maqsood, I.H. Gul, M. Anis-Ur-Rehman, Mater. Res. Bull. **87**, 177 (2017)

23. M.M. El-Nahass, A.A.M. Farag, A.A. Atta, Synth. Met. **159**, 589 (2009)

24. H.M. Zeyada, F.M. El-Taweel, M.M. El-Nahass, M.M. El-Shabaan, Chin. Phys. B **25**, 77701 (2016)

25. N.A. El-Ghamaz, A.Z. El-Sonbati, M.A. Diab, A.A. El-Bindary, M.K. Awad, S.M. Morgan, Mater. Sci. Semicond. Process. **19**, 150 (2014)

26. A. Omar, A.F. Qasrawi, N.M. Gasanly, J. Alloys Compd. **724**, 98 (2017)

27. A.K. Zak, W.H.A. Majid, M.E. Abrishami, R. Youse, Solid State Sci. **13**, 251 (2011)

28. B.S. Prabhu, Y.T. Rao, K.V. Kumar, V.S.S. and Kumari, World J. Nano Sci. Eng. **4**, 21 (2014)

29. H.M. Zeyada, H.M. El-Mallah, T. Atwee, D.G. El-Damhogi, Spectrochim. Acta Part A Mol. Biomol. Spectrosc. **179**, 120 (2017)

30. H.M. Zeyada, M.M. Makhlouf, Opt. Mater. (Amst). **54**, 181 (2016)

31. A.M. Nasr, H.I.A. El-kader, M. Farhat, Thin Solid Films **515**, 1758 (2006)

32. M.M. El-Nahass, H.M. Zeyada, M.S. Aziz, M.M. Makhlouf, Spectrochim. Acta Part A Mol. Biomol. Spectrosc. **62**, 11 (2005)

33. M.M. El-Nahass, K.F. Abd-El-Rahman, A.A. Al-Ghamdi, A.M. Asiri, Phys. B Condens. Matter **344**, 398 (2004)

34. J.N. Zemel, J.D. Jensen, R.B. Schoolar, Phys. Rev. 140, (1965)

35. S.H. Wemple, M. DiDomenico, Phys. Rev. B **3**, 1338 (1971)

36. A.S. Hassanien, J. Alloys Compd. **671**, 566 (2016)

37. A.S. Hassanien, A.A. Akl, J. Non. Cryst. Solids **432**, 471 (2016)

38. M.M. El-Nahass, A.F. El-Deeb, H.E.A. El-Sayed, A.M. Hassanien, Phys. B Condens. Matter **388**, 26 (2007)

39. H. Han, C. Davis, J.C. Nino, J. Phys. Chem. C **118**, 9137 (2014)

40. A.L. Efros, B.I. Shklovskii, J. Phys. C Solid State Phys. **8**, 1 (1975)

41. M.G. Hutchins, O. Abu-Alkhair, M.M. El-Nahass, K. Abdel-Hady, J. Non. Cryst. Solids **353**, 4137 (2007)

42. G.H. Jonker, J. Phys. Chem. Solids **9**, 165 (1959)

43. S. Matsumura, A.R. Hlil, C. Lepiller, J. Gaudet, D. Guay, Z. Shi, S. Holdcroft, A.S. Hay, Am. Chem. Soc. Polym. Prepr. Div. Polym. Chem. **49**, 511 (2008)

44. H.M. Zeyada, M.M. El-Nahass, M.M. El-Shabaan, Philos. Mag. **96**, 1150 (2016)

45. A.A.A. Darwish, M. Rashad, S.R. Alharbi, Appl. Phys. A **124**, 447 (2018)

46. H.Z.M. El-Nahass, N. El-Ghamaz, A. El-ghandour, Opt. Int. J. Light Electron Opt. (2018)

47. S. Obayya, N.F. Areed, M.F. Hameed, M.H. Abdelrazik, Innov. Mater. Syst. Energy Harvest. Appl. (In L. Mescia, O. Losito, & F. Prudenzano (Eds.), (2015), pp. 26–62

48. M.H. Muhammad, M.F.O. Hameed, S.S.A. Obayya, IEEE Photon. J. **9**, (2017)

49. S.S.A. Obayya., M. Hussein, K.R. Mahmoud, M.F.O. Hameed, J. Photon. Energy **8**, 22502 (2017)

50. S.A. Aly, A.A. Akl, Chalcogenide Lett. **12**, 489 (2015)

51. M. Pandiaraman, N. Soundararajan, C. Vijayan, J. Ovonic Res. **7**, 21 (2011)

52. N.-K. Persson, M. Sun, P. Kjellberg, T. Pullerits, O. Inganäs, J. Chem. Phys. **123**, 204718 (2005)

53. M. Hussein, K.R. Mahmoud, M.F.O. Hameed, S.S.A. Obayya, J. Photon. Energy **8**, 1 (2017)

54. Y.M. El-Toukhy, M. Hussein, M.F.O. Hameed, S.S.A. Obayya, Plasmonics **13**, 503 (2018)

55. Y.M. El-Toukhy, M. Hussein, M.F.O. Hameed, A.M. Heikal, M.M. Abd-Elrazzak, S.S.A. Obayya, Opt. Express **24**, A1107 (2016)